Journal of
Materials Chemistry A

ROYAL SOCIETY
OF CHEMISTRY

PAPER

View Article Online
View Journal | View Issue

Cite this: *J. Mater. Chem. A*, 2024, **12**, 9017

Single-step synthesis of titanium nitride-oxide composite and AI-driven aging forecast for lithium–sulfur batteries†

Ka Chun Li,[a] Xuanming Chen,[a] Aghil Sabbaghi,[b] Chi Ho Wong,*[c] Chak-yin Tang,*[d] Frank Leung-Yuk Lam*[a] and Xijun Hu*[a]

Received 11th January 2024
Accepted 8th March 2024

DOI: 10.1039/d4ta00234b

rsc.li/materials-a

In this study, the polysulfide shuttle effect, a major impediment to the efficiency of lithium–sulfur (Li–S) batteries, is addressed. A titanium nitride-oxide (TiO_2–TiN) composite is synthesized *via* a single-step liquid-phase reaction at 60 °C only, significantly streamlining the production for large-scale applications. This composite, serving as a cathode material in Li–S batteries, demonstrates remarkable performance, with an initial capacity of 774 mA h g^{-1}, and maintains 517 mA h g^{-1} after 500 cycles at a 0.5C rate with a decay rate of 0.066% per cycle. The integration of a Super P carbon-coated separator further enhances the battery performance, achieving an initial capacity of 926 mA h g^{-1} and maintaining 628 mA h g^{-1} after 500 cycles, with the lower decay rate of 0.064% per cycle. Moreover, the integration of Long Short-Term Memory (LSTM) networks into data analysis has facilitated the creation of a deep learning-based predictive model. This model is adept at accurately forecasting the aging effects of batteries up to 100 cycles in advance. This AI-driven approach represents a novel paradigm in battery research, offering the potential to expedite the battery testing process and streamline quality control procedures. Such advancements are pivotal in making the commercialization of Li–S batteries more feasible and efficient.

Introduction

Lithium–sulfur (Li–S) batteries are garnering significant attention as a promising candidate for next-generation energy storage solutions, primarily due to their exceptional theoretical energy density. The anode, made of lithium, boasts a theoretical capacity of 3860 mA h g^{-1}, while the sulfur cathode offers a capacity of 1672 mA h g^{-1}. In addition to their high energy potential, the abundant availability of sulfur makes it a cost-effective material for battery production.

Despite these advantages, the widespread commercialization of Li–S batteries faces a major challenge due to the ‘polysulfide (LiPS) shuttle’ phenomenon. This issue arises during the battery's discharge cycle. Initially, the sulfur cathode comprises a ring structure containing eight sulfur atoms. Through the process of chemical reduction, this ring structure gets fragmented, leading to the generation of various polysulfide ions. These ions, being soluble, can easily migrate through conventional polymer-based separators and reach the lithium anode. This migration not only reduces the active sulfur mass involved in redox reactions but also contributes to the formation of a deleterious layer on the anode, impeding the battery's performance. Consequently, this phenomenon presents a significant barrier to achieving the full theoretical potential of Li–S batteries.

To address the persistent challenge of the polysulfide shuttle effect in Li–S batteries, researchers have developed various innovative approaches. A notable strategy involves the use of metal oxides known for their polar properties, which serve as effective adsorbents. These materials capture polysulfides at the cathode *via* Lewis-acid interactions.[1] Key examples include SnO_2,[2] MnO_2,[3] Al_2O_3,[4] and Fe_2O_3,[5] and TiO_2.[6]

Titanium compounds are increasingly preferred for their environmental and safety benefits.[7] These compounds, characterized by low toxicity, offer a more sustainable alternative to other metals. The ready availability of titanium, coupled with its lower ecological impact during extraction and processing, aligns well with global sustainability initiatives. Additionally, the inherent stability of titanium compounds enhances battery safety by mitigating hazardous reactions, thereby improving overall battery performance and aligning with the push towards safer, more sustainable energy storage solutions.[8]

---

[a] *Department of Chemical and Biological Engineering, The Hong Kong University of Science and Technology, Clear Water Bay, Hong Kong S.A.R., China. E-mail: kexhu@ust.hk*

[b] *Department of Chemistry, Virginia Tech, Blacksburg, Virginia 24061, USA*

[c] *Department of Physics, The Hong Kong University of Science and Technology, Clear Water Bay, Hong Kong S.A.R., China*

[d] *Department of Industrial and Systems Engineering, The Hong Kong Polytechnic University, Kowloon, Hong Kong S.A.R., China*

† Electronic supplementary information (ESI) available. See DOI: https://doi.org/10.1039/d4ta00234b

Recent studies have highlighted the role of oxygen vacancies in TiO_2, which appear to catalyze polysulfide reactions, thereby facilitating the formation of S^{3-} radicals.[9] However, the application of TiO_2 for this purpose has been an uphill struggle. Its inherently insulating nature necessitates the integration of additional conductive materials or the design of specialized structures to enhance conductivity. This requirement can lead to increased production costs.[1,6,10,11] In search of alternatives, titanium carbide (TiC) has been identified as a potential material for the cathode, prized for its superior electroconductivity, essential for efficient electron transport. But this advantage is offset by a drawback, TiC exhibits weaker dipole interactions, diminishing its affinity for LiPS and thereby potentially compromising the battery's ability to adsorb polysulfides, a key factor in ensuring long-term stability and capacity. To strike a balance between electroconductivity and adsorption efficiency, researchers have been exploring intermediate materials. These materials aim to combine the beneficial properties of both TiO_2 and TiC. Notably, composite materials, consisting of TiO_2 and TiC, have shown promise in enhancing the overall performance of Li–S batteries.[12,13]

Another material garnering interest in Li–S battery research is titanium nitride (TiN) which is recognized for its great catalytic influence in polysulfide conversion. Its exceptional polarization effect is the key to ensuring rapid redox kinetics, a crucial aspect for efficient battery operation.[14] Despite the potential of TiN, as highlighted in various studies,[14–16] its synthesis often entails complex procedures under harsh conditions, such as the use of hazardous hydrogen fluoride[17] or exposure to extreme temperatures.[18] These factors make TiN less practical for large-scale applications.

This study introduces an innovative approach for synthesizing a titanium nitride-oxide composite (TiO_2–TiN), ingeniously combining the high lithium polysulfide (LiPS) adsorption capacity of TiO_2 with the superior electroconductivity of TiN through a simplified, single-step liquid-phase reaction. Departing from conventional multi-step methods that rely on high-temperature processes and ammonia usage,[19,20] which require sealed environments, the developed method significantly reduces associated financial and environmental burdens. By eliminating the need for toxic ammonia and high temperature, it decreases production costs and lessening the ecological footprint and greenhouse gas emissions, in alignment with sustainability goals. Moreover, avoiding high-temperature conditions and the handling of hazardous gases significantly enhances workplace safety. Therefore, this innovative process presents a safer, more environmentally friendly, and cost-effective alternative for fabricating TiO_2–TiN composites, demonstrating a commitment to environmental preservation and the safety of occupational environments.

Additionally, the integration of a Super P-coated separator presents a simple and cost-effective approach to enhance battery performance, which effectively deter the formation of polysulfides.[21–23] It is anticipated that this combination will lead to significant improvements in decay rates and capacities, effectively addressing the polysulfide shuttle phenomenon in a manner that is both practical and efficient for large-scale applications.

Besides the challenges in Li–S (Li–S) battery production, the extensive time required for battery testing, particularly cyclic charge/discharge performance assessments, presents a significant obstacle. The duration of these tests typically extends over several weeks to months, which prolongs the overall duration of research and quality testing, thereby increasing the associated time costs.

To address this challenge, the integration of advanced AI algorithms, specifically Long Short-Term Memory (LSTM) networks, is proposed. These networks are adept at identifying and addressing errors related to the aging effects in Li–S batteries and are particularly suited for forecasting battery aging due to their ability to process and learn from sequential data. The application of these aging forecasts could significantly reduce the duration of battery testing, thereby enhancing the efficiency of Li–S battery commercialization.

Experimental methods

Preparation of TiO_2–TiN composite and TiO_2–TiN/S composite

To synthesize the TiO_2–TiN composite, commercial TiN underwent liquid phase oxidation *via* an etching reaction. The etchant, a mixture of 68–69% nitric acid and absolute ethanol (1 : 4 by volume), was prepared. A gram of TiN was introduced to 150 ml of this solution and magnetically agitated for 12 h in a 60 °C water bath. Post-reaction, the composite was filtered, washed with distilled water and ethanol, and dried in a 70 °C oven overnight. The TiO_2–TiN/S composite was synthesized using melt-diffusion. The TiO_2–TiN composite and sublimated sulfur (in a 1 : 3 weight ratio) were amalgamated through high-energy ball milling for over 4 h. This mixture was then placed in a tube furnace within a quartz boat. With argon protection, the furnace was set to ramp up to 155 °C at 3 K min^{-1}, sustaining this temperature for 12 h. Following this, the sample underwent further grinding using ball milling, yielding the "TiO_2–TiN/S composite". For comparative evaluation, the same procedure was executed using TiN, generating the TiN/S composite (Fig. 1).

Preparation of carbon-coated separator

A mixture of carbon (Super P) and polyvinylidene difluoride (PVDF (6 : 4 by weight)) was dissolved in NMP and ball-milled at 400 rpm for 5 h. Using the doctor blade method, this slurry was

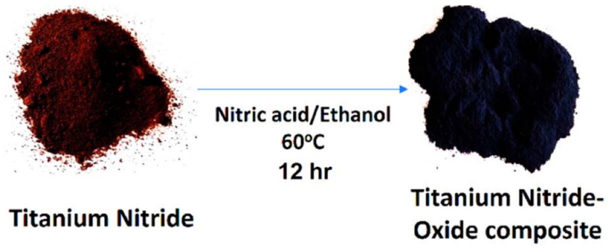

Fig. 1 Illustration of the synthesis of TiO_2–TiN composite.

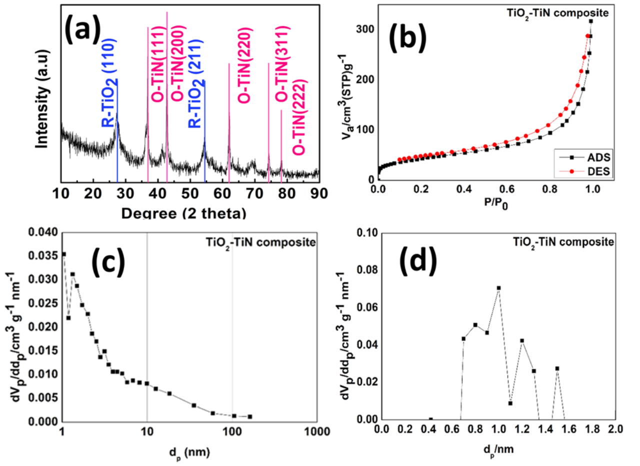

Fig. 2 (a) The XRD pattern, (b) adsorption–desorption isotherm, (c) BJH plot and (d) MP plot of TiO_2–TiN composite.

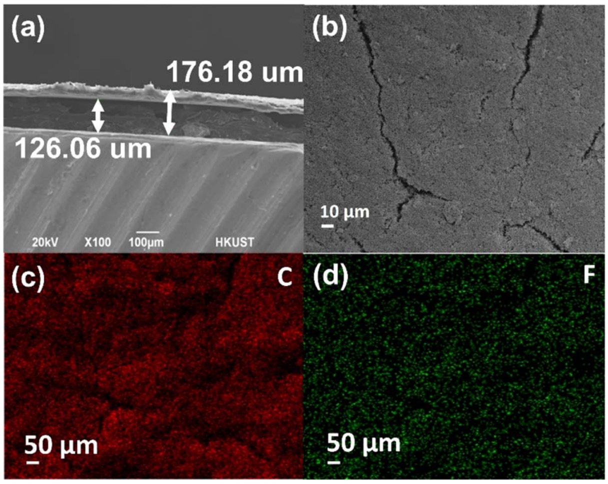

Fig. 4 SEM images of (a) the cross-sectional view of the super P coated separator, (b) the front view of the super P coated separator (500×), (c and d) and the corresponding elemental mapping.

spread uniformly on a Celgard 2325 separator. Post-coating, the separator was dried in a vacuum oven at 60 °C overnight and subsequently trimmed into a 19 mm diameter disc, ensuring a material deposition of roughly 0.5 mg cm^{-2}.

Polysulfide adsorption test

Based on the previous research[24,25] a comparative polysulfide adsorption experiment for TiO_2–TiN composites and commercial TiN was conducted. A 4×10^{-3} M Li_2S_6 solution was prepared by dissolving proportions of sulfur and Li_2S (5 : 1 molar ratio) in a 1 : 1 v/v 1,2-dimethoxyethane (DME)/1,3-dioxolane (DOL) solution, yielding a deep orange solution after 48 h of magnetic stirring. Thereafter, 30 mg of each cathode material and 2.5 ml Li_2S_6 solution were combined in clear containers to start the adsorption. Each solution was first stirred for 10 min and then allowed to stabilize within the glove box.

Thermogravimetric analysis (TGA)

The thermal stability of the TiO_2–TiN composite was determined using thermogravimetric analysis. This analysis was conducted in an argon atmosphere, with the temperature being gradually increased from 25 °C to 200 °C at a rate of 5 °C min^{-1}.

Scalability validation test

To validate the scalability of the proposed single-step liquid-phase reaction for synthesizing the TiO_2–TiN composite, an expanded experiment was conducted. The synthesis was scaled up incrementally from 1 g of TiN in 150 ml of etching solution to ratios of 2 g/300 ml, 4 g/600 ml, and eventually 10 g/1.5 L. The resulting products were collected and analysed with XRD and nitrogen adsorption–desorption analysis.

Electrochemical measurements and characterization

The cathode slurries, consisting of the cathode materials, MWCNT, and PVDF in a 7 : 2:1 weight ratio, were mixed with 1-methyl-2-pyrrolidone (NMP) to form a homogeneous paste. This paste was then uniformly spread onto aluminum foil using the doctor blade method, dried at 60 °C overnight, and punched into 12 mm diameter discs. CR2025 Li–S coin cells were

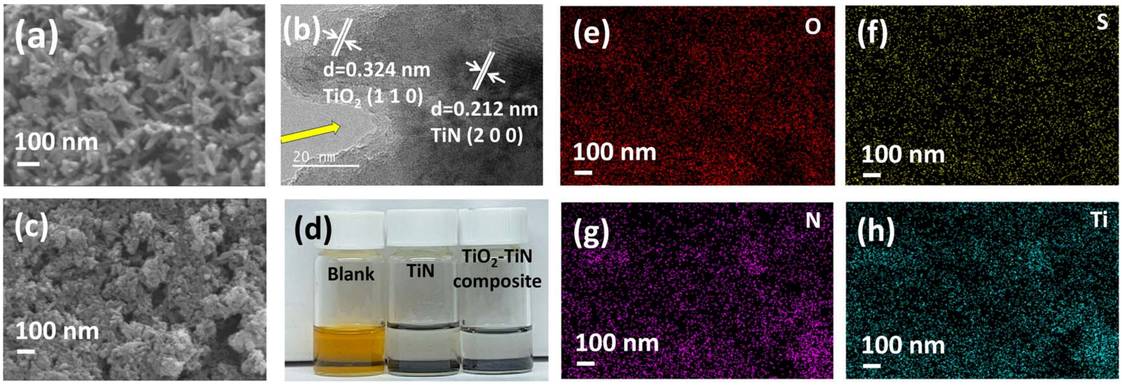

Fig. 3 (a) SEM image, (b) TEM images, (c) SEM images, (d) the visual adsorption experiment of TiO_2–TiN composite and (e–h) the corresponding elemental mapping.

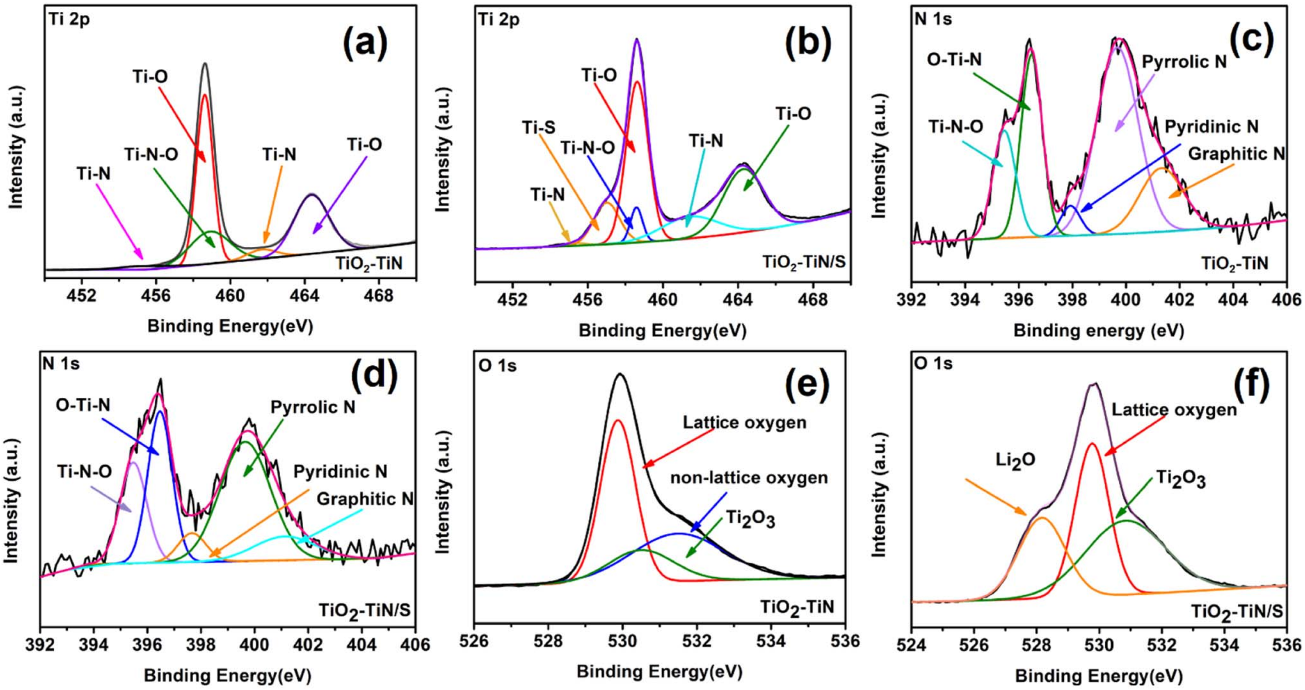

Fig. 5 XPS spectra for (a) TiO_2–TiN composite Ti 2p, (b) TiO_2–TiN composite/S Ti 2p, (c) TiO_2–TiN composite N 1s, (d) TiO_2–TiN composite/S N 1s, (e) TiO_2–TiN composite O 1s, (f) TiO_2–TiN composite/S O 1s.

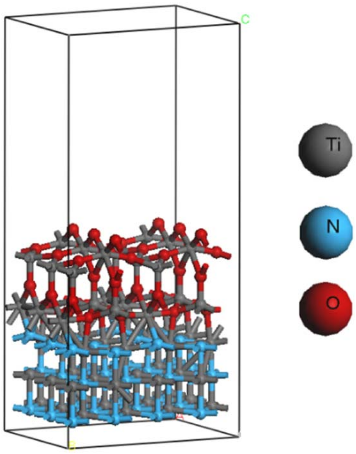

Fig. 6 DFT model of the TiO_2–TiN composite. A repeating unit is drawn.

assembled in an argon-rich glove box with the processed cathode, lithium foil anode, and either the Celgard 2325 separator or the carbon-coated variant. The electrolyte was a 1 : 1 v/v solution of 1,2-dimethoxyethane (DME) and 1,3-dioxolane (DOL) supplemented with 1 M lithium bis(trifluoromethanesulfone)imide and 0.1 M $LiNO_3$. Each cell was loaded with ~20 μL of the electrolyte (40 μL if carbon-coated separator is used). Galvanostatic analyses of the assembled cells were performed between 1.7 and 2.8 V using a CT4008T cell tester (NEWARE, China). In addition, CV scans of the cells were captured using an electrochemical workstation (CH instrument, China) within the 1.7–2.8 V voltage window. Sample morphologies were investigated through Scanning Electron Microscopy (SEM, JEOL-6390F) and Transmission Electron Microscopy (TEM, JEM 2010F). X-ray diffraction (XRD, PW1830) and nitrogen (N_2) adsorption–desorption isotherms (MicrotracBEL BELSORP MAX G) were applied to analyze the ordered structure of the samples. X-ray Photoelectron Spectroscopy (XPS, Physical Electronics 5600) was used with a monochromatic Al Kα source to ascertain the chemical composition of the samples.

DFT calculations

A reverse derivation method has been applied to construct a DFT model of the actual TiO_2–TiN composite. Starting with real X-ray diffraction (XRD) data, individual layers of TiN and TiO_2 are initially modelled. These layers are then systematically modified, including changes in atomic positions and crystal planes, to align the simulated XRD pattern with the actual data, achieving a weighted profile R-factor (R_{wp}) of less than 15%. This method allows the direct simulation of the composite, as opposed to relying on the side deductions typical of previous studies. The creation of a realistic model of the intermediate compound by this method represents a significant advancement in the field. The accuracy of simulations is not only enhanced but also the need for multiple experimental tests is reduced, thereby streamlining the research process. The calculations were executed using the CASTEP. In our study, the Generalized Gradient Approximation (GGA) within the Perdew–Burke–Ernzerhof (PBE) scheme was utilized,[26,27] along with ultra-soft pseudopotentials, to conduct the calculations. For TiN, TiO_2, or TiO_2–TiN composite, a vacuum distance exceeding

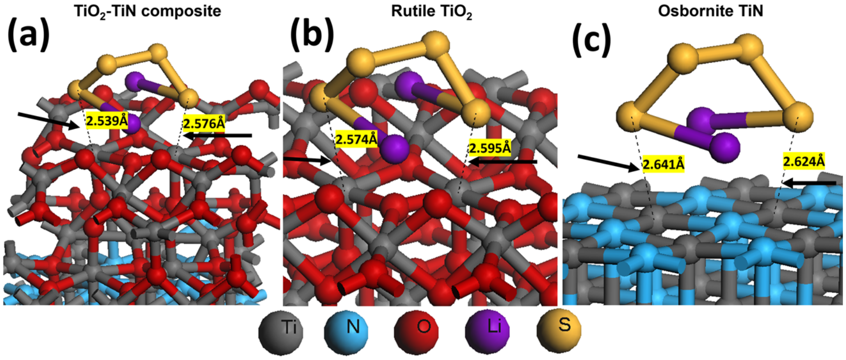

Fig. 7 Optimized geometries illustrating the adsorption of Li_2S_4 by (a) the local region of TiO_2–TiN composite, (b) R-TiO_2 and (c) O–TiN with their corresponding Ti–S bonds.

10 Å was maintained to negate interactions between consecutive slabs.[28] The cutoff energy for the projector augmented plane-wave basis set stands at 400 eV.[29,30] The set threshold for self-consistent field iterations is 1×10^{-6} eV per atom.[31,32] The adsorption energy (E_a) for Li_2S_4 on either the TiN or TiO_2 surface is defined as $E_{ads} = E_{total} - E_{Li_2S_4} - E_{surf}$, where the E_{total} is the total energy of the adsorbed system, the $E_{Li_2S_4}$ represents the energy of Li_2S_4 in a vacuum and the E_{surf} is the energy of the optimized clean TiN, TiO_2, or TiO_2–TiN heterostructure surface slab.[33]

AI method

In this study, the TiO_2–TiN/S batteries were utilized for the AI modelling. For the analysis, voltage data was measured experimentally as a function of time during both charge and discharge processes. This data was subsequently loaded into the MATLAB environment for deeper analysis and interpretation. A complete cycle is defined as the combination of voltage–time data during the charging process, followed by voltage–time data during the discharging process. To eliminate the warm-up phase, the first 24 cycles were excluded from the training data. Instead, the training was given to data from the 25th to the 100th cycle, which was aligned in a time series format and utilized as the training set. The LSTM network was employed to generate simulated charge and discharge curves at the 200th cycle. Through the examination of features extracted from the data forecasted for the 200th cycle, the specific sources of error for each region were identified. This analysis allowed us to observe how different LSTM parameters helped to mitigate these errors on a regional basis.

Results and discussion

The XRD patterns of the TiO_2–TiN composite in Fig. 2a clearly delineate the characteristic peaks of both Rutile TiO_2 (R-TiO_2) and Osbornite TiN (O–TiN). Specifically, the (110) and (211) peaks indicate the presence of R-TiO_2, while the (111), (200), (220), (222), and (311) peaks confirm O–TiN. SEM and TEM provide insights into the morphology and microstructure of the composite.

Through the BET analysis, the BET area and pore volume as 155.27 $m^2\ g^{-1}$ and 0.87 $cm^3\ g^{-1}$, respectively. This porous structure amplifies the interaction with sulfur, optimizing its utilization and offering superior adsorption sites for polysulfides. The hysteresis loop of the composite, categorized as type IV(a) by IUPAS and illustrated in Fig. 2b, corroborates the

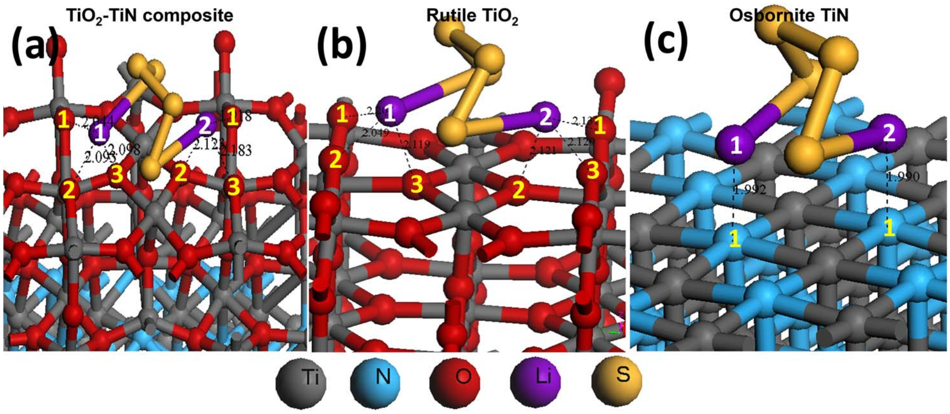

Fig. 8 Optimized geometries illustrating the adsorption of Li_2S_4 by (a) TiO_2–TiN composite, (b) R-TiO_2 with their corresponding Li–O bond and (c) O–TiN with its Li–N bonds.

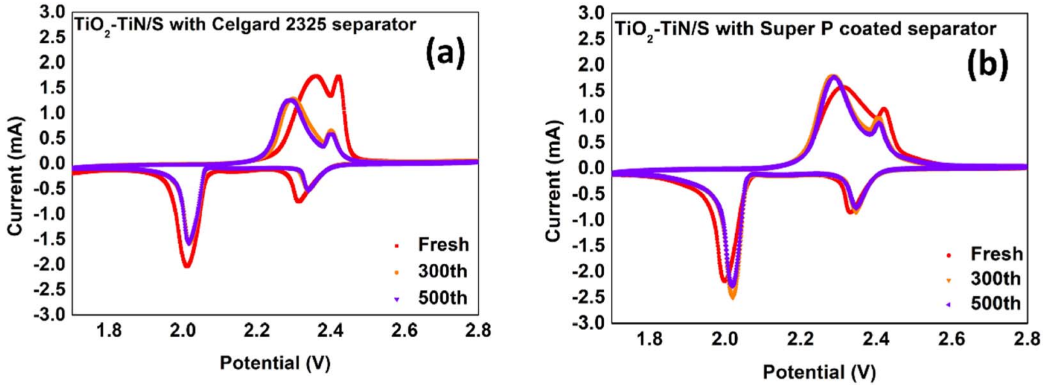

Fig. 9 (a) The CV curves of TiO_2–TiN/S battery with Celgard 2325 separator, (b) TiO_2–TiN/S battery with carbon coated separator.

presence of slit-like pores within the material.[12] The BJH plot in Fig. 2c highlights a peak presence of pores in the 2–10 nm range, with a minor peak presence between 10 and 20 nm. The MP plot in Fig. 2d emphasizes the microporous nature of the composite, spotlighting pore diameters ranging from 0.7 nm to 1.5 nm. All these observations confirm the existence of slit-like pores in the TiO_2–TiN composite. The composite has an average pore size of 15.2 nm, optimal for sulfur storage and apt for accommodating volume changes during Li_2S_4 and Li_2S transitions.

To validate the scalability of the proposed single-step liquid-phase reaction for synthesizing the TiO_2–TiN composite, scalability validation tests were conducted. The XRD results (Fig. S1, ESI†) shows consistent peak positions for composites produced at different scales, confirming their identical chemical compositions and affirming the process's scalability by demonstrating that increased production volumes do not compromise the TiO_2–TiN composite's integrity. Furthermore, nitrogen adsorption–desorption analyses provided additional evidence that upscaling the reaction does not adversely affect the product's

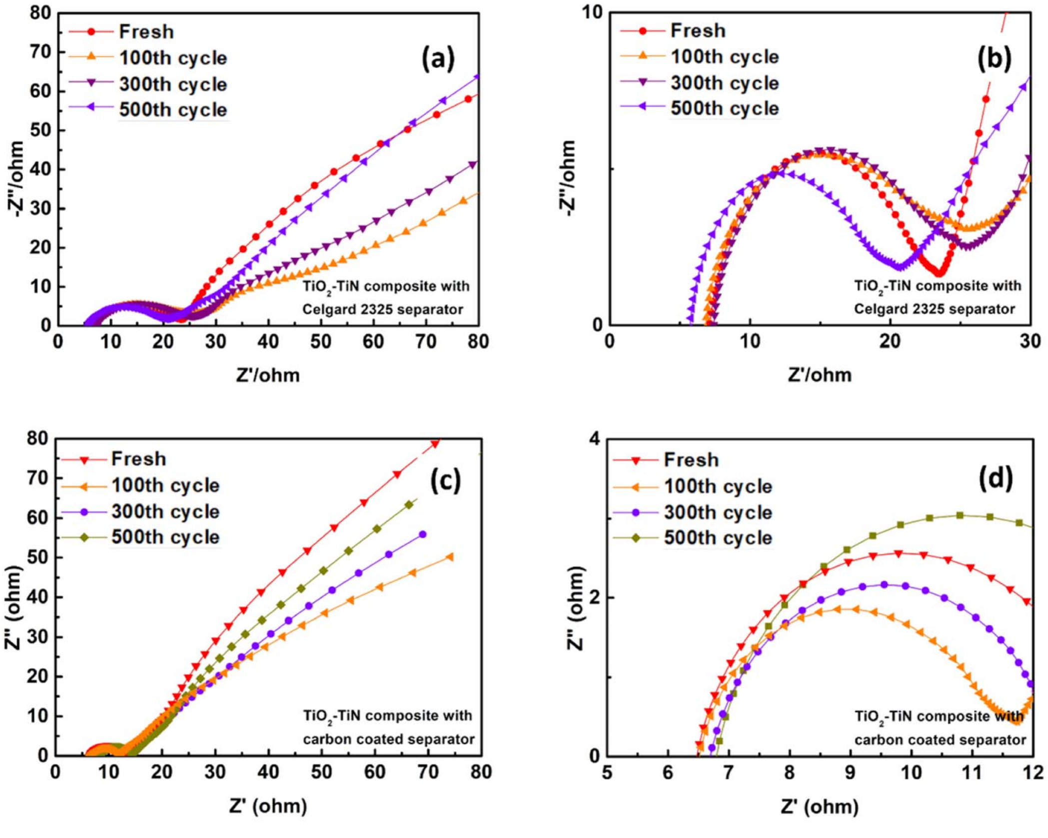

Fig. 10 Nyquist plots of (a and b) TiO_2–TiN/S battery with Celgard 2325 separator and (c and d) TiO_2–TiN/S battery with carbon coated separator.

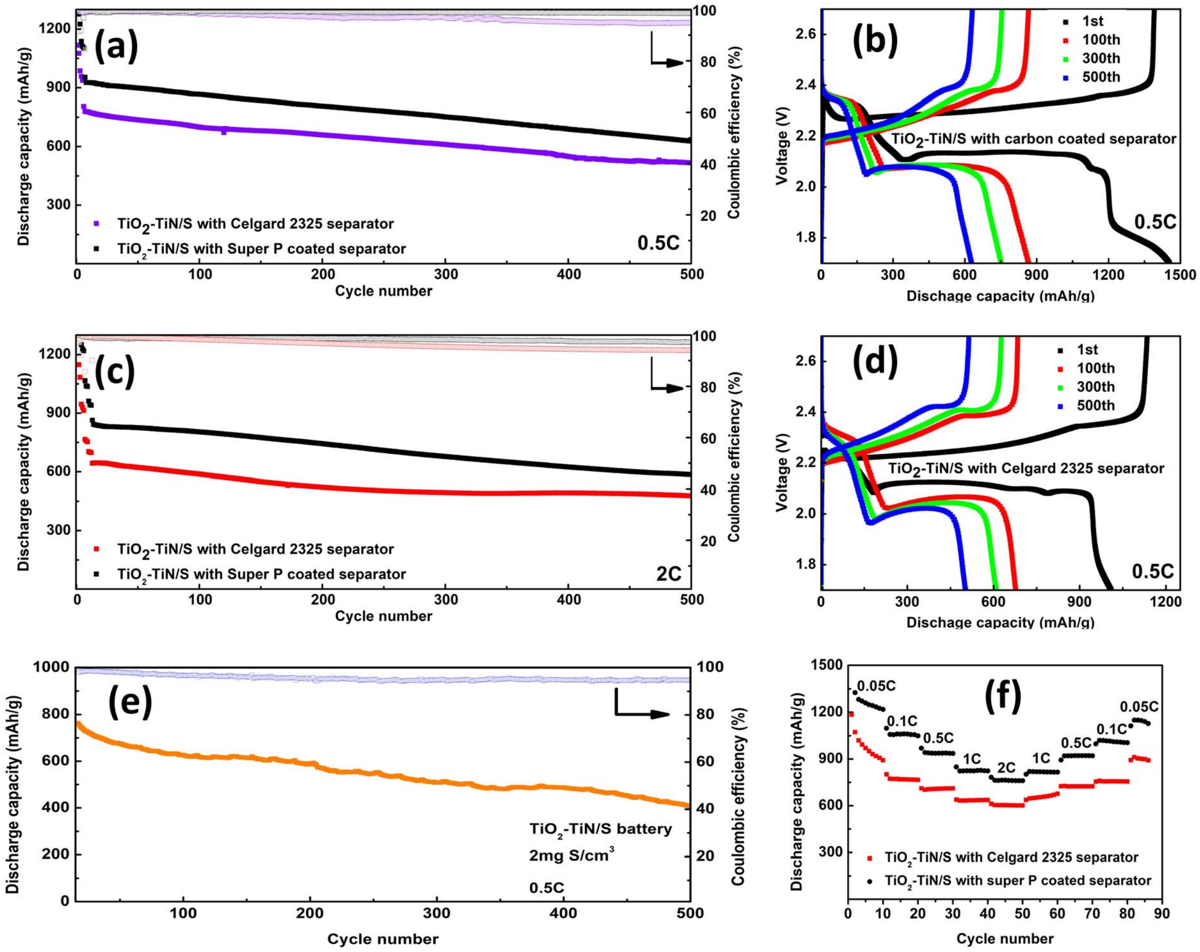

Fig. 11 Electrochemical performance of Li–S batteries. (a) Cyclic performance test on the TiO_2–TiN/S battery with carbon coated separator and Celgard 2325 separator in 0.5C, (b) charge–discharge profiles of TiO_2–TiN/S battery with carbon coated separator at different cycle numbers in 0.5C, (c) cyclic performance test on the TiO_2–TiN/S battery with carbon coated separator and Celgard 2325 separator in 2C, (d) discharge–charge profiles of TiO_2–TiN/S battery with Celgard 2325 separator at different cycle numbers in 0.5C, (e) cyclic performance test on TiO_2–TiN/S battery with Celgard 2325 separator with 2.0 mg sulfur loading, and (f) rate performances of TiO_2–TiN/S battery from 0.05C to 2C.

integrity. The isotherms and BJH plots (Fig. S2, ESI†) for TiO_2–TiN composites produced at varying scales shows negligible differences, further substantiating the process's suitability for large-scale applications and its commercial production viability.

The SEM imaging reveals a unique sponge-like structure formed by leaf-like particles in the TiO_2–TiN composite, as seen in Fig. 3a. After undergoing the melt-diffusion process with sulfur, the composite surface exhibited a smoother appearance, suggesting successful sulfur incorporation, as depicted in Fig. 3c. Elemental mapping further confirms the uniform distribution of sulfur within the composite, illustrated in Fig. 3e.

TEM analysis offers a detailed understanding of the dual-layered structure of the composite surface. Two lattice patterns can be discerned in Fig. 3b, the outer shell, defined by a 0.324 nm lattice fringe, corresponds to the (110) plane of rutile TiO_2, while the inner core features a 0.24 nm lattice fringe corresponding to the (200) plane of O–TiN. A clear pore with the diameter about 20 nm is displayed in Fig. 3b which aligns with the nitrogen adsorption–desorption findings. An adsorption experiment, executed within an argon-secured glove box,

Table 1 The selected LSTM parameters for the training data

	Setting A (see Fig. 12b)	Setting B (see Fig. 13a)	Setting C (see Fig. 13b)	Setting D (see Fig. 13c)
Gradient threshold	0.5	0.1	0.1	0.1
Initial learning rate	0.001	0.001	0.003	0.003
Learning rate (drop factor)	0.2	0.2	0.2	0.62

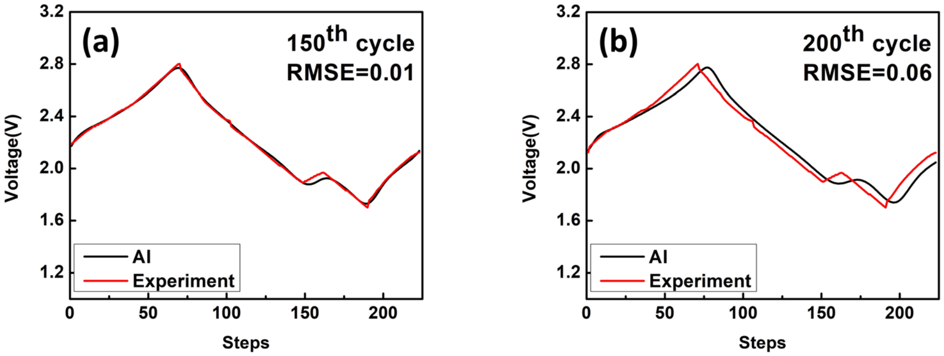

Fig. 12 The training data is collected from 25th to 100th cycle. (a) The comparison between the AI prediction and experimental charge and discharge curves at the 150th cycle. (b) The same comparison but at the 200th cycle. The LSTM parameters are referred to setting A in Table 1.

revealed that the TiO_2–TiN composite possessed a superior adsorption capability compared to commercial TiN, evident from Fig. 3d. This pronounced adsorption efficiency arises from the elevated concentration of TiO_2 in the composite.

The TGA analysis was performed in an argon atmosphere, covering a temperature range from room temperature to 200 °C (Fig. S3, ESI†). This range encompasses the standard operational temperatures of Li–S batteries, which typically do not exceed 70 °C,[34] as well as the melt-diffusion process conducted at 155 °C. The evaporation of residual ethanol and water, together with the decomposition of organic residues, accounted for a weight loss of approximately 7.7% [35] when the temperature increased to 200 °C. Notably, the absence of any abrupt weight reductions within this temperature range indicates that there were no phase changes or decomposition of the composites. This stability suggests that the TiO_2–TiN composite does not undergo significant thermal degradation or other reactions that might compromise its structural integrity. Most of the residues evaporate during the melt-diffusion process at 155 °C, ensuring that they do not impact the performance of Li–S batteries. Consequently, the TiO_2–TiN composite is deemed suitable for utilization in Li–S batteries, as it serves as a stable host material for sulfur. It is unlikely to contribute to capacity loss or pose safety risks due to thermal instability under standard or slightly elevated operating conditions.

The carbon-coated separator underwent SEM analysis, complemented by elemental assessment *via* the EDX technique. The cross-sectional view of the carbon-coated separator in Fig. 4a indicates the Celgard 2325 separator possesses a thickness close to 126 μm, while the Super P coating measures around 50 μm, marking a 39.75% thickness increased due to the coating. The top view of the carbon coated separator in Fig. 4b presents a consistent distribution of Super P carbon with some interspersed minor cracks. Such features underscore its capacity to curtail lithium polysulfide diffusion. The void space of Super P carbon particles creates interconnected pathways, bolstering electrolyte infiltration and electron transport, which in turn amplifies electrochemical performance.[36] The uniform Super P carbon layer facilitates efficient electron movement, reactivating trapped active materials during battery cycling,[37] and preventing inactive precipitate formation. Moreover, the distinctive sponge-like structure of super P inhibits the emergence of non-conductive agglomerates.[21]

EDX elemental mapping detected not only the carbon signal from Super P but also fluorine, attributed to the binder, polyvinylidene fluoride. In addition to its adhesive role, fluorine aids in polysulfide adsorption, ensuring their confinement to the cathode and safeguarding the lithium metal anode.[38]

The XPS spectra are presented in Fig. 5a–f. Fig. 5a reveals the presence of a Ti–N–O peak, indicating that the material is a composite of TiN and TiO_2 rather than a mere mixture. Upon completion of the adsorption test, the adsorbents were collected post-adsorption testing and subjected to XPS characterization. XPS spectra of the TiO_2–TiN/S composite in Fig. 5b display all

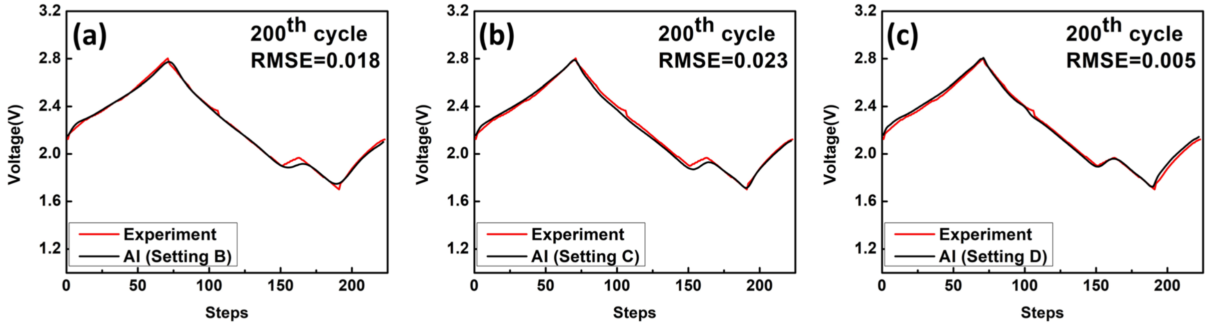

Fig. 13 The impact of tuning various LSTM parameters on the accuracy of AI prediction for the 200th cycle. The three variable parameters under consideration are (a) the gradient threshold; (b) the initial learning rate; (c) the drop factor of learning rate.

the characteristic peaks of the TiO_2–TiN composite. A peak at 456.9 eV corresponding to the Ti–S bond, signifying both the material's chemisorption of polysulfides and its ability to trap polysulfides.[39] This Ti–S bond might originate from the sulfur atom of the polysulfide trapped in the oxygen vacancy, underscoring the catalytic role of the oxygen vacancy in the polysulfide redox reaction.[39] The N 1s spectrum of TiO_2–TiN, illustrated in Fig. 5c, detects five nitrogen peaks: the Ti–N–O bond at 395.6 eV,[38] the O–Ti–N bond at 396.4 eV,[40] pyridinic N at 397.9 eV,[41] pyrrolic N at 399.7 eV,[41] and graphitic N at 401.5 eV.[41] Both graphitic N and pyridinic N play pivotal roles in the electron transfer during the redox reaction. The dipole–dipole interaction between pyridinic N and polysulfides further accentuates the catalytic reaction.[42] Fig. 5d retains a consistent pattern with all primary peaks of the TiO_2–TiN composite evident in the N 1s spectrum of the TiO_2–TiN/S composite. In Fig. 5e, the O 1s XPS spectrum for the TiO_2–TiN composite is fitted with peaks at binding energies of 529.9 eV,[43] 530.3 eV,[43] and 531.3 eV,[43,44] representing lattice oxygen, Ti_2O_3, and non-lattice oxygen respectively.[43] The emergence of Ti_2O_3 and non-lattice oxygen peaks suggest oxygen vacancies within the lattice.[43] An analysis of the O 1s XPS spectrum of TiO_2–TiN/S in Fig. 5f identifies three peaks with binding energies at 528.1 eV,[45] 529.7 eV,[43] and 530.3 eV.[43] The latter two binding energies, synonymous with the peaks before adsorption, denote lattice oxygen and Ti_2O_3. A peak shift is observed for lattice oxygen in the XPS analysis. The shift to a lower binding energy, from 529.9 eV to 529.7 eV, typically indicates an increase in electron density around the oxygen atoms. This could be due to the presence of electron-rich sulfur species on the material's surface. The interaction between these sulfur species and the TiO_2–TiN composite might increase the electron density of the lattice oxygen. Notably, the new peak at 528.1 eV indicates the bond formation with Li_2O,[45] further attesting to the polysulfide adsorption capability. The vanishing non-lattice oxygen peak at 531.3 eV likely results from the ion-exchange process wherein the sulfur of polysulfide molecules supplants the non-lattice oxygen.

The concurrent observation of distinctive patterns associated with both TiO_2 and TiN components was significantly demonstrated by the results of Raman spectroscopy (Fig. S4 ESI†), providing clear evidence for the formation of TiO_2–TiN composite structures. The presence of four prominent peaks at approximately 153, 400, 520, and 635 cm^{-1} are corresponded to O–TiN.[46] The peaks at the lower frequencies, specifically at 153 and 400 cm^{-1}, are attributed to the vibrations of acoustical phonons,[46] while the peaks observed at the higher frequencies of 520 and 635 cm^{-1} are attributed to the vibrations of optical phonons.[46] In contrast, the Raman shifts at 143, 235, 447, and 612 cm^{-1} are attributed to the B_{1g} mode,[47] two-phonon scattering,[47] E_g mode,[47] and A_{1g} mode[47] of the R-TiO_2, respectively. The characteristic peaks of both TiO_2 and TiN are discerned in the TiO_2–TiN composite. These peaks exhibit shifts, including overlapping signals between the R-TiO_2 and O–TiN.[48] Such shifts caused by the disparities in crystal structures or lattice constants between the constituent phases, which are common phenomena in composites. These phenomena indicate that the lattice vibrations are influenced by the strain in the TiO_2–TiN composite.[48] These alterations in the Raman peaks, in conjunction with the XPS results that reveal the existence of a Ti–N–O peak in the Ti 2p spectrum (see Fig. 5a) as well as both Ti–N–O and O–Ti–N bonds in the N 1s spectrum (see Fig. 5d), further validate the existence of the TiO_2–TiN composite. This evidence reveals the complex interaction between TiO_2 and TiN, thereby distinguishing the composite state from a simple mixture state.

DFT modeling, alongside surface science characterization techniques such as XRD and XPS, is employed to analyze the interaction between the TiO_2–TiN composite and LiPS. The challenge in constructing a DFT model for the TiO_2–TiN composite arises from the incomplete oxidation reaction inherent in its synthesis, complicating the determination of precise atomic coordinates. To address this, a reverse derivation method was developed, allowing the modification of TiO_2 and TiN layers within the model and enabling the simulation of XRD patterns until they closely matched with the actual XRD data. Typically, a model is considered accurate if the simulated XRD pattern has a R_{wp} less than 15% compared to the actual pattern. By altering and simulating different crystal planes of R-TiO_2 and O–TiN, it was found that the combination of TiO_2(1 1 0) and TiN(2 0 0) crystal planes could construct a TiO_2–TiN composite model with a notably low R_{wp} of 11.28% (Fig. S5, ESI†).

Building on the TiO_2–TiN composite model established through DFT, the CASTEP module is utilized for further simulations. To assess the adsorption affinity of different materials to lithium polysulfides (LiPS), Li_2S_4, a representative of LiPS, is introduced into the system containing the materials under study (R-TiO_2, O–TiN, and the TiO_2–TiN composite). The interaction between Li_2S_4 and these materials is allowed to evolve until the system reaches its lowest energy state. This state is indicative of the most stable configuration of the system. By measuring the bond lengths within this configuration, particularly the Ti–S and Li–O bonds, insights into the interaction strength between the materials and Li_2S_4 can be gained. Shorter bond lengths correspond to lower system energy and, consequently, stronger adsorption affinity. This approach enables a comparative analysis of how R-TiO_2, O–TiN, and the TiO_2–TiN composite interact with LiPS, thereby determining their effectiveness in mitigating the polysulfide shuttle effect in Li–S batteries.

In-depth analysis of the adsorption process was conducted using the CASTEP module, as illustrated in Fig. 6a and S1–S3.† This analysis focused on the attractive forces between titanium and sulfur in Li_2S_4 and lithium with oxygen (or nitrogen in the case of TiN). These forces, reflected in the atomic distances, are inversely proportional to the intensity of attraction. The simulation reveals that in the TiO_2–TiN composite model, two titanium-sulfur (Ti–S) bonds with Li_2S_4 are present, with Ti–S distances measured at 2.539 Å and 2.576 Å (average 2.558 Å, see Fig. 7a). Comparatively, for R-TiO_2, the distances are 2.574 Å and 2.595 Å (average 2.585 Å, see Fig. 7b), while the O–TiN model shows distances of 2.641 Å and 2.624 Å (average 2.633 Å, see Fig. 7c). The TiO_2–TiN composite, thus, exhibits a shorter average Ti–S distance, indicating a stronger attraction potential.

Moreover, the interaction between lithium from Li_2S_4 and the oxygen or nitrogen atoms in the composite materials is significant. The TiO_2–TiN and R-TiO_2 models both have two lithium atoms coordinated by three adjacent oxygen atoms (Fig. 8a and b), while the O–TiN model has only one adjacent nitrogen atom per lithium (Fig. 8c), suggesting weaker interactions compared to the Li–O bonds in the TiO_2–TiN and R-TiO_2 composites. The bond lengths of Li–O in the TiO_2–TiN composite are 2.044 Å, 2.093 Å, 2.098 Å, 1.918 Å, 2.123 Å, and 2.183 Å, averaging 2.077 Å. In the R-TiO_2 model, the Li–O bond lengths are 2.207 Å, 2.049 Å, 2.119 Å, 2.121 Å, 2.120 Å, and 2.131 Å, with an average of 2.125 Å. The TiO_2–TiN composite shows shorter average Li–O bond lengths, implying stronger adsorption affinity to LiPS compared to R-TiO_2.

To investigate the different affinities to the Li_2S_4 from TiO_2–TiN composite and R-TiO_2, Electron Density Difference (EDD) analysis was also performed. It is a technique used to understand changes in electron distribution within a material or molecule. It elucidates the charge redistribution within the TiO_2–TiN composite during interaction and identify regions of electron accumulation and depletion (Fig. S6, ESI†). This analysis reveals that interaction predominantly occurs between the inner TiN layer and the outer TiO_2 layer, with a transfer of electrons from TiO_2 to TiN. This electron migration enhances the positive charge on the TiO_2 surface, thereby increasing its ability to adsorb electron-rich LiPS. The robust adsorption affinity of the TiO_2–TiN composite is further supported by both the shortest average Ti–S bond length and Li–O bonds, as well as the simulated adsorption energy data. The TiO_2–TiN composite demonstrates a notable energy change of −3.35 eV upon adsorption, compared to −3.16 eV for R-TiO_2, and −2.69 eV for O–TiN, thus confirming its superior adsorption affinity to Li_2S_4.

A series of electrochemical experiments were conducted to examine the electrochemical performance of the TiO_2–TiN composite as a cathode material for Li–S batteries. Fig. 9 presents the cyclic voltammetry (CV) curves of the Li–S batteries utilizing a TiO_2–TiN composite as sulfur host, demonstrates the superior performance of the composite and discovers the role of the carbon-coated separator. All curves exhibit the characteristic four redox peaks associated with Li–S batteries, comprising two reduction peaks and two oxidation peaks. During the cathodic scan, the reduction peaks centered at approximately 2.3 V signify the conversion of sulfur to high-ordered polysulfides (long-chain polysulfides). The peaks centered around 2.0 V pertain to the further reduction of high-ordered polysulfides to low-ordered polysulfides (short-chain polysulfides), ultimately resulting in Li_2S_4/Li_2S.[49] Conversely, during the anodic scan, the oxidation peaks near 2.3 V represent the transformation of low-ordered polysulfides back to high-ordered polysulfides. The peaks around 2.45 V signify the oxidation of high-ordered polysulfides to sulfur. From the morphology of the peaks, freshly assembled batteries exhibit higher and broader peaks, which could likely result from signals attributed to the initial material activation processes. Conversely, the CV curves of the TiO_2–TiN batteries, after 300 and 500 cycles, are seen to largely overlap. However, the TiN/S battery displays two diminishing peaks (Fig. S7 ESI†). This suggests the enhanced reversibility for the TiO_2–TiN/S battery, primarily attributed to the outermost TiO_2 layer's ability to trap polysulfides, thereby minimizing the shuttle effect. Notably, the peaks of the TiO_2–TiN/S battery are slightly narrower than those of the TiN/S battery, suggesting higher electron transfer. This might be due to the enhanced polysulfides adsorption capacity of the composite, which holds the polysulfide close to the sulfur host surface, thus shortening the electron transfer distance.

When comparing the CV curves of the TiO_2–TiN/S battery using a standard Celgard 2325 separator to the one with a carbon-coated separator, the most pronounced observation is the increased peak height provided by the latter battery, suggesting enhanced redox kinetics, mostly because of the enhanced conductivity of the cathode. With the carbon coated separator, electrons can transfer through an alternative path, which traverses through the carbon layer of the coated separator, and subsequently reaches the cathode.

Electrochemical impedance spectroscopy (EIS) measurements were conducted for the TiO_2–TiN/S battery to understand the kinetics of the electrochemical reactions. The Nyquist plots of the TiO_2–TiN/S batteries with Celgard 2325 separator and carbon coated separator are depicted in Fig. 10. A Nyquist plot typically features a depressed semicircle in the high-frequency region and a sloping line in the low-frequency region. These respectively correspond to the charge transfer resistance (R_{ct}) between the electrode and the electrolyte, and the Warburg impedance (Z_w) associated with diffusion processes in the electrode material. The starting point of the curves (R_s, the intersection point between the first semicircle and the real axis in the high-frequency region) represents the series resistance (R_s), which includes the ionic resistance of the electrolyte as well as other resistances in the cell such as the resistance of the current collectors and the intrinsic resistance of the electrode materials.[50] The impedance spectra of all the cells, both fresh and cycled, consistently exhibit a single depressed semicircle in the high-frequency region, followed by a sloping line in the low-frequency region. Notably absent from these plots is the second depressed semicircle, which is typically indicative of additional resistance due to the deposition of inactive and insulating Li_2S_4/Li_2S. This feature is commonly observed in the Nyquist plots of standard Li–S batteries.[51] The absence of this second semicircle in our plots provides compelling evidence of the superior catalytic performance of TiO_2–TiN composite materials. Specifically, it suggests that the high surface area of the TiO_2–TiN composite inhibits inactive Li_2S_4/Li_2S formation on the cathode surface. This is a significant finding, as the deposition of these inactive and insulating compounds can severely hinder battery performance by increasing resistance and limiting ion transport. Furthermore, the absence of the second semicircle in the cycled cells indicates that this beneficial effect is maintained over multiple charge–discharge cycles. This suggests that the TiO_2–TiN composite materials not only improve the initial performance of the Li–S batteries but also contribute to their long-term stability and durability.

By comparing the cathode materials, TiO_2–TiN composite and TiN, as illustrated in Fig. 10a and b and S8, ESI.† It can be observed that the series resistance (R_s) from the TiO_2–TiN/S battery is slightly lower than that from the TiN/S battery. This could be because the TiO_2–TiN composite has a higher surface area than TiN. A higher surface area can lead to a larger contact area for the electrolyte, facilitating electron transport and thereby reducing the resistance. However, after cycling, the R_s values of both batteries shift to the right, indicating an increase in resistance. Interestingly, the magnitude of this shift of TiO_2–TiN/S battery is significantly smaller than TiN/S battery. The superior performance in terms of maintaining low resistance during cycling of the TiO_2–TiN composite can be attributed to its enhanced polysulfide trapping ability compared to TiN alone. This is primarily due to the presence of surface TiO_2 in the composite, which strongly interacts with polysulfides. This interaction inhibits the dissolution of polysulfides, thereby preventing an increase in electrolyte viscosity.[50] The charge transfer resistance (R_{ct}) of the cells, discernible from the size of the depressed semicircle in the high-frequency region of the Nyquist plot, indicates the resistance at the electrode–electrolyte interface.

Fresh cells exhibit a larger depressed semicircle, suggesting a higher R_{ct}. This can be attributed to factors such as an unbalanced sulfur distribution on the cathode surface, it could lead to inefficient utilization of active materials or formation of insulating layers, thereby increasing the charge transfer resistance.[52] After 100 cycles, the size of the depressed semicircles decreases, reflecting a reduction in the material interface resistance and implying the electrochemical activation of the active materials. Notably, the increase in R_{ct} for the TiO_2–TiN/S battery is negligible, while the R_{ct} of the TiN/S battery increases with the number of cycles (as evidenced by the enlargement of the depressed semicircles in the high-frequency region). The presence of TiO_2 in the TiO_2–TiN composite material results in a stronger affinity for polysulfides in the heterostructures, a characteristic not observed in bare TiN. This strong affinity effectively stabilizes the interfacial resistance between the electrode and the electrolyte,[53] thereby promoting the utilization efficiency of sulfur during cycling. This observation aligns with previous reports on similar cathode materials.[48,53] The stabilized series resistance and R_{ct} of the TiO_2–TiN/S battery contribute to improved cyclic stability, corroborating the results of the cyclic charge–discharge performance tests discussed in subsequent sections.

For the TiO_2–TiN/S battery with a carbon-coated separator, it retains all the advantages of the TiO_2–TiN/S battery, but exhibits a smaller R_s and R_{ct}. This suggests that the carbon-coated separator can further reduce the battery's internal resistance, potentially because of the alternative electron pathway from the electron shell to the cathode.

Fig. 11a illustrates the cyclic performance comparison between the TiO_2–TiN/S batteries equipped with a carbon-coated separator and a Celgard 2325 separator at a 0.5 charge–discharge rate (current density, C rate). In the initialization at 0.05C, the battery using the carbon-coated separator begins with a capacity of 1422 mA h g^{-1}, whereas the one with the Celgard 2325 separator starts at a lower discharge capacity of 1010 mA h g^{-1}. At 0.5C, the curves for both batteries are nearly parallel. The carbon-coated separator battery commences with a capacity of 926 mA h g^{-1} and maintains 628 mA h g^{-1} after 500 cycles, resulting in an average decay rate of 0.064% per cycle. In contrast, the battery with the Celgard 2325 separator begins at 774 mA h g^{-1}, ending at 517 mA h g^{-1} after the same number of cycles, with an average decay rate of 0.066% per cycle. Both batteries consistently exhibit a coulombic efficiency exceeding 95%, underscoring the composite's excellent control over polysulfides. Similar trends were observed during the cyclic performance test of the batteries at a 2C rate, as depicted in Fig. 11c. Two near-parallel curves emerge. The battery with carbon-coated separator begins at 864 mA h g^{-1} and retains 586 mA h g^{-1} after 500 cycles. In comparison, the battery with the Celgard 2325 separator starts at 699 mA h g^{-1} and maintains 464.23 mA h g^{-1} after the same number of cycles. The average decay rates for these batteries are 0.064% and 0.067%, respectively. These findings suggest that introducing a Super P coated separator to the TiO_2–TiN/S battery may not significantly suppress the polysulfide shuttle, likely because the composite intrinsically has robust polysulfide adsorption capabilities. The function of the Super P coated separator lies in enhancing the cathode's overall conductivity and optimizing the conversion of active material, including the conversion of polysulfides species. This contributes to a higher discharge capacity and sustained battery performance, even at elevated C rates. Moreover, the carbon coating further stabilizes the stability of the interface between the separator and electrodes. This can help prevent the formation of unstable passivation layers that could impair ion transport and lead to performance degradation at high C rates, thus further protecting the battery at a high C rate.

The influence of the TiO_2–TiN composite, coupled with the support of the carbon-coated separator, on polysulfides conversion was further assessed by measuring polarization potential, the voltage difference between charging and discharging. A smaller polarization potential indicates diminished internal resistance and improved reaction kinetics, while a larger value suggests the opposite.[54] The measurements were taken at half the specific capacity during the charge and discharge processes of the 100th cycle at 0.5C. Comparative measurements revealed polarization values of 0.196 V for the TiO_2–TiN/S battery with a carbon-coated separator and 0.264 V for the one with the Celgard 2325 separator, as shown in Fig. 11b & d. The noticeably smaller polarization in the battery with the carbon-coated separator suggests a more efficient redox reaction of lithium polysulfides. This indicates that the interface reactions of the carbon-coated separator markedly enhance the redox reaction, significantly reducing the formation and buildup of insulating materials on the cathode's surface.

Fig. 11e illustrates the cyclic performance of the TiO_2–TiN/S battery with a higher sulfur loading (2 mg). The discharge capacity remains stable, with a retention rate of approximately 60% after 500 cycles and a small average decay rate of 0.10% per cycle over 500 cycles. This indicates that a higher sulfur loading rate does not significantly decrease the polysulfide control ability of the material.

Fig. 11f illustrates the rate capability of the TiO_2–TiN/S batteries equipped with both carbon-coated and Celgard 2325 separators across varying currents. The TiO_2–TiN/S battery with the carbon-coated separator demonstrates robust discharge capacities of 1326 mA h g^{-1}, 1097 mA h g^{-1}, 969 mA h g^{-1}, 848 mA h g^{-1}, and 782 mA h g^{-1} at current densities of 0.05C, 0.1C, 0.5C, 1C, and 2C, respectively. When cycling back to initial current densities in subsequent cycles, the battery retains rate capabilities of 83.8%, 92.7%, 94.8%, and 94.4% at 0.05C, 0.1C, 0.5C, and 1C, respectively. In a parallel assessment, the TiO_2–TiN/S battery with the Celgard 2325 separator yielded discharge capacities of 1072 mA h g^{-1}, 801 mA h g^{-1}, 711 mA h g^{-1}, 639 mA h g^{-1}, and 611 mA h g^{-1} at the same respective current densities. Its rate capabilities stood at 83.3%, 94.0%, 102%, and 99.6% for 0.05C, 0.1C, 0.5C, and 1C, respectively. The elevated rate capability of the TiO_2–TiN/S battery is attributed to the harmonious interaction between the highly electroconductive TiN and the potent polysulfide-trapping properties of TiO_2. This synergy ensures proficient electrochemical reactions throughout the system.

The evaluation of battery performance, particularly through cyclic charge–discharge tests, is inherently time-consuming. Completing a sufficient number of cycles to assess performance can take several weeks, and even months if lower C-rates are involved. This extended duration of testing can decrease the efficiency of battery performance evaluation. Luckily, AI can be leveraged to predict the aging effects of Li–S batteries, potentially shortening the time required for extensive battery testing, and therefore offers a promising solution to this challenge.

Among various AI models, LSTM networks[55] are particularly advantageous. Their capability to remember long-term dependencies is crucial for battery performance prediction, where past cycles significantly influence future performance. The LSTM can effectively capture and analyze these dependencies, which makes it a powerful tool in predicting the battery's life span and efficiency, thereby enhancing the overall process of battery performance evaluation. In this study, the LSTM network was utilized to predict the aging effects in the TiO_2–TiN/S battery with a Super P coated separator. The root-mean-square error (RMSE),[56] analyzed as a function of the epoch number, indicated that a plateau in RMSE reduction was securely reached at the 500th epoch. Consequently, this duration was selected for the LSTM training, as documented in Table 1. Predictions of charge and discharge curves for future cycles by the LSTM, illustrated in Fig. 12a and b, where one step equates to approximately 30 seconds. Discrepancies at the 150th cycle primarily emerged between steps 150 and 170 due to kink features, corresponding to the polysulfide transition phase, as indicated by the model. At the 200th cycle, a significant increase in errors was observed, resulting in an RMSE sixfold higher than at the 150th cycle. These findings highlight the challenges in accurately predicting extended cycling behavior and the complex chemical transitions occurring within the battery.

To enhance the predictive accuracy of the LSTM network, an extensive optimization of its parameters was undertaken, the details of which are summarized in Table 1. This optimization process involved implementing a piecewise learning rate schedule,[57] setting the maximum number of epochs at 500, and adjusting the drop period to 120 epochs. The objective of testing different values for each parameter was to assess their impact on predictive accuracy and identify the most effective settings for the AI model. Notably, adjusting the gradient threshold, as evidenced in the comparison between Fig. 12b and a, proved instrumental in maintaining high accuracy in predictions, except in discontinuous regions. Further refinement of the initial learning rate effectively addressed discrepancies observed around step 190 (Fig. 13b). The optimized predictions, as shown in Fig. 13c, demonstrated a closer alignment with the experimental data, highlighting the success of these parameter adjustments in improving the LSTM model's forecasting capabilities.

The fine-tuning aimed to address this localized inaccuracy, and the resulting improvements illustrate how these adjustments enhanced the model's precision in this critical step range, reducing the previously observed errors and thereby improving the overall forecasting reliability of the LSTM network. By manipulating the selected parameters of the LSTM model, accurate forecasting of battery performance at the 200th cycle was not only achieved, but it was also discovered that these parameters played a critical role in minimizing the forecasting error for battery curves up to the 200th cycle. The comprehensive optimization of the LSTM parameters played a pivotal role in enhancing the AI's predictive accuracy for the battery's charging and discharging cycles. By modulating the initial learning rate, the model achieved faster convergence and effectively circumvented potential stalls at local optima, thereby refining its predictive accuracy. Additionally, setting an appropriate gradient threshold was instrumental in preventing issues such as exploding or vanishing gradients, contributing to stable model training and improved prediction fidelity. Furthermore, the careful calibration of the learning rate's drop factor facilitated finer adjustments in the model's parameter updates as it neared convergence. This approach prevented oscillations around the optimal solution, ensuring consistent and precise predictions throughout the training process, which is crucial for accurately forecasting battery behavior.

Conclusions

In this research, the TiO_2–TiN composite was synthesized through a single-step liquid-phase reaction, showing its scalability and practicality for large-scale production. The method for fabricating TiO_2–TiN composites introduced in this study reduces costs and energy use, enhances safety, and minimizes environmental impact, offering a more efficient, safer, and sustainable alternative. Demonstrated in Li–S batteries, the composite exhibited superior performance as a cathode material, effectively mitigating the polysulfide shuttle effect, and maintaining high capacity and stability. With the application of a Super P coated separator, an enhancement in battery performance was observed. In addition, the application of AI, particularly LSTM networks, was explored for predicting the aging effects in Li–S batteries. This novel application provided significant insights into the battery's performance over time, shortening the time required for battery testing, and thus making the commercialization of Li–S batteries more feasible and efficient.

Author contributions

Ka Chun Li and Xuanming Chen contributed equally: investigation, performing the experiment, data collection, writing, and manuscript revising. Aghil Sabbaghi: revising the manuscript. Xuanming Chen: DFT calculation. Chi Ho Wong: supervision, AI calculation, manuscript revising. Xijun Hu: supervision, manuscript revising. Frank L. Y. Lam: supervision, manuscript revising. Chak-yin Tang: supervision, manuscript revising. The manuscript was written through contributions of all authors. All authors have given approval to the final version of the manuscript.

Conflicts of interest

There are no conflicts to declare.

Acknowledgements

We appreciate the technical assistance from Materials Characterization & Preparation Facility (MCPF) at HKUST.

Notes and references

1 A. Singh and V. Kalra, *ACS Appl. Mater. Interfaces*, 2018, **10**, 37937.
2 L. P. Zhang, Y. F. Wang, S. Q. Gou and J. H. Zeng, *J. Phys. Chem. C*, 2015, **119**, 28721.
3 X. Liang and L. F. Nazar, *ACS Nano*, 2016, **10**, 4192.
4 M. Yu, W. Yuan, C. Li, J. D. Hong and G. Shi, *J. Mater. Chem. A*, 2014, **2**, 7360.
5 C. Zheng, S. Niu, W. Lv, G. Zhou, J. Li, S. Fan, Y. Deng, Z. Pan, B. Li, F. Kang and Q. H. Yang, *Nano Energy*, 2017, **33**, 306.
6 Z. Wei Seh, W. Li, J. J. Cha, G. Zheng, Y. Yang, M. T. McDowell, P.-C. Hsu and Y. Cui, *Nat. Commun.*, 2013, **4**, 1331.
7 K. Ronoh, F. Mwema, S. Dabees and D. Sobola, *Biomed. Eng. Adv.*, 2022, **4**, 100047.
8 A. Markowska-Szczupak, M. Endo-Kimura, O. Paszkiewicz and E. Kowalska, *Nanomaterials*, 2020, **10**, 1.
9 Y. Li, X. Li, Y. Hao, A. Kakimov, D. Li, Q. Sun, L. Kou, Z. Tian, L. Shao, C. Zhang, J. Zhang and X. Sun, *Front. Chem.*, 2020, **8**, 309.
10 E. H. M. Salhabi, J. Zhao, J. Wang, M. Yang, B. Wang and D. Wang, *Angew. Chem., Int. Ed.*, 2019, **58**, 9078.
11 Z. Xiao, Z. Yang, L. Wang, H. Nie, M. Zhong, Q. Lai, X. Xu, L. Zhang and S. Huang, *Adv. Mater.*, 2015, **27**, 2891.
12 Z. Cui, J. Yao, T. Mei, S. Zhou, B. Hou, J. Li, J. Li, J. Wang, J. Qian and X. Wang, *Electrochim. Acta*, 2019, **298**, 43.
13 X. Zhang, W. Yuan, Y. Yang, Y. Chen, Z. Tang, C. Wang, Y. Yuan, Y. Ye, Y. Wu and Y. Tang, *Small*, 2020, **16**, 2005998.
14 X. Gao, D. Zhou, Y. Chen, W. Wu, D. Su, B. Li and G. Wang, *Commun. Chem.*, 2019, **2**, 1.
15 Y. Lu, Y. Wang, W. Wang, Y. Guo, Y. Zhang, R. Luo, X. Liu and T. Peng, *J. Phys. D: Appl. Phys.*, 2019, **52**, 025502.
16 H. You, M. Shi, J. Hao, H. Min, H. Yang and X. Liu, *J. Alloys Compd.*, 2020, **823**, 153879.
17 Z. Li, J. Zhang, B. Guan, X. W. Lou, D. Li, J. T. Zhang, D. Y. Guan and X. W. Lou, *Angew. Chem., Int. Ed.*, 2017, **56**, 16003.
18 Z. Cui, C. Zu, W. Zhou, A. Manthiram and J. B. Goodenough, *Adv. Mater.*, 2016, **28**, 6926.
19 Y. Q. Cao, X. R. Zhao, J. Chen, W. Zhang, M. Li, L. Zhu, X. J. Zhang, D. Wu and A. D. Li, *Sci. Rep.*, 2018, **8**, 1.
20 Y. Liu, J. Zhang, Q. Liu and X. Li, *RSC Adv.*, 2020, **10**, 37209.
21 D. Zhao, X. Qian, L. Jin, X. Yang, S. Wang, X. Shen, S. Yao, D. Rao, Y. Zhou and X. Xi, *RSC Adv.*, 2016, **6**, 13680.
22 S. H. Chung and A. Manthiram, *J. Phys. Chem. Lett.*, 2014, **5**, 1978.
23 S.-H. Chung and A. Manthiram, *Adv. Funct. Mater.*, 2014, **24**, 5299.
24 Q. Sun, B. He, X. Q. Zhang and A. H. Lu, *ACS Nano*, 2015, **9**, 8504.
25 W. Chen, T. Qian, J. Xiong, N. Xu, X. Liu, J. Liu, J. Zhou, X. Shen, T. Yang, Y. Chen and C. Yan, *Adv. Mater.*, 2017, **29**, 1605160.
26 W. Cui, S. Yu and J. Zhao, *Comput. Mater. Sci.*, 2020, **171**, 109228.
27 D. Ma, B. Hu, W. Wu, X. Liu, J. Zai, C. Shu, T. Tadesse Tsega, L. Chen, X. Qian and T. L. Liu, *Nat. Commun.*, 2019, **10**, 3367.
28 H. Pan, *J. Phys. Chem. C*, 2014, **118**, 9318.
29 R. Tang, R. Zhang, C. Shi, E. Liu and N. Zhao, *Int. J. Electrochem. Sci.*, 2023, **18**, 100289.
30 G. Li, X. Wang, M. H. Seo, M. Li, L. Ma, Y. Yuan, T. Wu, A. Yu, S. Wang, J. Lu and Z. Chen, *Nat. Commun.*, 2018, **9**, 1.
31 Q. Zhang, X. Zhang, Y. Xiao, C. Li, H. H. Tan, J. Liu and Y. Wu, *ACS Omega*, 2020, **5**, 29272.
32 M. Fang, J. Han, S. He, J. C. Ren, S. Li and W. Liu, *J. Am. Chem. Soc.*, 2023, **145**, 12601.
33 T. Zhou, W. Lv, J. Li, G. Zhou, Y. Zhao, S. Fan, B. Liu, B. Li, F. Kang and Q.-H. Yang, *Energy Environ. Sci.*, 2017, **10**, 1694.
34 H. Zhang, J. Chen, Z. Li, Y. Peng, J. Xu and Y. Wang, *Adv. Funct. Mater.*, 2023, **33**, 2304433.
35 A. Bera, P. Hajra, S. Shyamal, H. Mandal, D. Sariket, S. Kundu, S. Mandal and C. Bhattacharya, *Mater. Today: Proc.*, 2018, **5**, 10161.
36 Y. Wang, X. Li, X. Hu, Y. An, Z. Ni, H. Cheng, Y. Wang, Z. Yang, Y. Zhang, Y. Zhang and Y. Zhang, *Int. J. Electrochem. Sci.*, 2020, **15**, 12633.
37 S. H. Chung and A. Manthiram, *Electrochim. Acta*, 2013, **107**, 569.
38 S. Banerjee, X. Han, M. A. Siegler, E. M. Miller, N. M. Bedford, B. C. Bukowski and V. S. Thoi, *Chem. Mater.*, 2022, **34**, 10451.
39 C. Qi, M. Cai, Z. Li, J. Jin, B. V. R. Chowdari, C. Chen and Z. Wen, *Chem. Eng. J.*, 2020, **399**, 125674.
40 B. Viswanathan and K. R. Krishanmurthy, *Int. J. Photoenergy*, 2012, **2012**, 269654.

41 P. Lazar, R. Mach and M. Otyepka, *J. Phys. Chem. C*, 2019, **123**, 10695.

42 Q. Shen, L. Huang, G. Chen, X. Zhang and Y. Chen, *J. Alloys Compd.*, 2020, **845**, 155543.

43 B. Bharti, S. Kumar, H. N. Lee and R. Kumar, *Sci. Rep.*, 2016, **6**, 1.

44 P. T. Hsieh, Y. C. Chen, K. S. Kao and C. M. Wang, *Appl. Phys. A*, 2008, **90**, 317.

45 E. K. W. Andersson, C. Sångeland, E. Berggren, F. O. L. Johansson, D. Kühn, A. Lindblad and J. Mindemark, *J. Mater. Chem. A*, 2021, **9**, 22462.

46 Y. Yue, P. Han, X. He, K. Zhang, Z. Liu, C. Zhang, S. Dong, L. Gu and G. Cui, *J. Mater. Chem.*, 2012, **22**, 4938.

47 S. F. Shaikh, R. S. Mane, B. K. Min, Y. J. Hwang and O. S. Joo, *Sci. Rep.*, 2016, **6**, 1.

48 C. Gong, C. Yan, J. Zhang, X. Cheng, H. Pan, C. Zhang, L. Yu and Z. Zhang, *J. Mater. Chem.*, 2011, **21**, 15273.

49 M. Wild and G. J. Offer, *Li-S Batteries*, John Wiley & Sons, Ltd, 2019.

50 A. Sabbaghi, C. H. Wong, X. Hu and F. L. Y. Lam, *J. Alloys Compd.*, 2022, **899**, 163268.

51 Z. Deng, Z. Zhang, Y. Lai, J. Liu, J. Li and Y. Liu, *J. Electrochem. Soc.*, 2013, **160**, A553.

52 W. Kong, L. Sun, Y. Wu, K. Jiang, Q. Li, J. Wang and S. Fan, *Carbon*, 2016, **96**, 1053.

53 T. Zhou, W. Lv, J. Li, G. Zhou, Y. Zhao, S. Fan, B. Liu, B. Li, F. Kang and Q.-H. Yang, *Energy Environ. Sci.*, 2017, **10**, 1694.

54 M. Zhao, B. Q. Li, X. Q. Zhang, J. Q. Huang and Q. Zhang, *ACS Cent. Sci.*, 2020, **6**, 1095.

55 K. Greff, R. K. Srivastava, J. Koutník, B. R. Steunebrink and J. Schmidhuber, *IEEE Transact. Neural Networks Learn. Syst.*, 2015, **28**, 2222.

56 T. Chai and R. R. Draxler, *Geosci. Model Dev.*, 2014, **7**, 1247.

57 H. Yang, J. Liu, H. Sun and H. Zhang, *IEEE Access*, 2020, **8**, 112805.